Available online at www.sciencedirect.com
SCIENCE DIRECT®
Journal of Magnetic Resonance 169 (2004) 39–48
JMR Journal of Magnetic Resonance
www.elsevier.com/locate/jmr

Improvement of homonuclear dipolar decoupling sequences in solid-state nuclear magnetic resonance utilising radiofrequency imperfections

Leon Bosman,[a,1] P.K. Madhu,[b] Shimon Vega,[a,*] and Elena Vinogradov[a,2]

[a] *Department of Chemical Physics, Weizmann Institute of Science, Rehovot 76100, Israel*
[b] *Department of Chemical Sciences, Tata Institute of Fundamental Research, Homi Bhabha Road, Colaba, Mumbai 400 005, India*

Received 29 December 2003; revised 31 March 2004
Available online 27 April 2004

Abstract

The often annoying imperfections in the phases and pulses of typical radiofrequency multiple-pulse irradiation schemes for homonuclear dipolar decoupling are revisited and analysed here. The analysis is with respect to one such multiple-pulse sequence, namely, the windowed phase-modulated Lee-Goldburg sequence. The error terms in the Hamiltonian due to pulse imperfections may lead to effective rotation of the spins around the *z*-axis giving rise to image free and high-resolution ^{1}H spectra. Certain precautions to be taken with regard to scale factor estimation are also detailed. The analysis also points out the range of off-set values where the best homonuclear dipolar decoupling performance of a particular pulse scheme may be obtained.

Keywords: Radiofrequency; Imperfections; Windowed PMLG; Proton spectra; Solid-state NMR

1. Introduction

High-resolution proton NMR spectroscopy of organic compounds and bio-molecules has become an integral part of modern solid-state NMR spectroscopy. Unlike the solution-state counterpart, in solids, proton NMR has been implemented only recently in two-dimensional (2D) spectroscopy [1–4]. Better theoretical understanding of the spin interactions under radiofrequency (RF) irradiation and magic-angle spinning (MAS) together with an improved performance of modern solid-state NMR spectrometers to apply accurate phase, amplitude and frequency modulation of RF irradiation are some of the reasons. The pulse sequences for ^{1}H–^{1}H homonuclear dipolar decoupling require these modulations as do many other multiple pulse schemes for decoupling or recoupling experiments [5].

The averaging of the dipolar interactions to near-zero in coupled proton systems is presently accomplished by combining MAS and RF irradiation, the latter being heralded by the Lee-Goldburg (LG) off-resonance RF irradiation [6], and by the near on-resonance multiple-pulse scheme WAHUHA [7,8]. While MAS averages the chemical shift anisotropy (CSA), the RF pulse sequences influence the dipolar interactions in spin space. Combination of the two, the CRAMPS experiments [9,10], has led to proton spectra narrowed to sub-ppm linewidths. At spinning frequencies of about 10 kHz the favourite decoupling techniques are FSLG [11] and PMLG [12–14], the *R*-symmetry based sequences [15], and DUMBO [16]. Although perhaps not always the most efficient, we have been using the phase-modulated LG (PMLG*n*) techniques, based on the frequency switched LG (FSLG) method, to obtain 1D and 2D proton spectra. The repeating pulse unit of this sequence consists of a set of short and constant amplitude pulses with varying phases. Detection windows can be inserted between the pulse units (*w*PMLG*n*) [17] and different numbers of 2*n* pulses can be chosen according to the RF amplitude and unit

* Corresponding author. Fax: +972-8-934-4123.
E-mail address: shimon.vega@wisemail.weizmann.ac.il (S. Vega).
[1] Deceased on February 23, 2003.
[2] Present address: Radiology Department, The Beth Israel Deaconess Medical Center, 330 Brookline Avenue, Boston, MA 02215, US.

1090-7807/$ - see front matter © 2004 Published by Elsevier Inc.
doi:10.1016/j.jmr.2004.04.001

length [13]. Since these pulse sequences are applied on rotating samples care must be taken at high spinning frequencies regarding the MAS and RF unit periods. The performance of *w*PMLG*n* has been studied theoretically using bimodal Floquet theory and has been shown experimentally on a variety of compounds [17]. These experimental results are strongly dependent on the accuracy of the pulse shapes, their phases and amplitudes. For example, inhomogeneities of the RF amplitude across the sample volume contribute significantly to the line broadening [8]. Other imperfections such as phase glitches and pulse dead-times can influence the spectra significantly. The effects of phase glitches have been discussed extensively in the past, as well as ways to reduce their influence on the spectra close to, and far off-resonance (second averaging) [18].

Direct detection of the proton signals by introducing short detection windows during the RF irradiation puts strong restrictions on the pulse sequences as well as on the RF probe design. Imperfections of the RF parameters are however inevitable in these experiments and they have been a source of many investigations leading to efforts undertaken to eliminate these errors or compensate for them [8,19,20]. A list of eight imperfections was identified by Haeberlen, namely, finite pulse widths, flip angle errors common to all pulses, RF inhomogeneity, power droop, flip angle errors different for the different set of pulses, phase errors, phase transients, and timing errors [8].

In this publication we will discuss the influence of RF phase and pulse imperfections on proton spectroscopy and show how we can benefit from these imperfections. We will focus on the effects of the experimental imperfections of the pulses composing the *w*PMLG*n* sequence, although the treatment and conclusions are valid for any homonuclear decoupling sequences. First, we will give a short description of the PMLG*n* decoupling scheme using an effective interaction Hamiltonian in order to provide a theoretical basis for the experimental observations. A simple vector representation will be given that defines the zero-order chemical-shift Hamiltonian of the distorted *w*PMLG*n* sequence. Simulated spectra will be shown displaying the effects of the pulse imperfections and finally experimental results will be presented that demonstrate the applicability of these effects.

2. The zero-order effective Hamiltonian

The homonuclear dipole–dipole (DD) decoupling experiment on a coupled proton spin system rotating at the magic-angle is described by a spin Hamiltonian in the rotating frame that can be divided into four terms: the dipolar spin Hamiltonian ($\mathcal{H}_{\mathrm{DD}}(t)$), the chemical-shift Hamiltonian ($\mathcal{H}_{\mathrm{CS}}(t)$), the Hamiltonian representing the ideal RF irradiation ($\mathcal{H}_{\mathrm{RF}}(t)$) and the error terms containing the RF imperfections ($\mathcal{H}_{\mathrm{E}}(t)$), and is given as (neglecting the weak scalar coupling)

$$\mathcal{H}(t) = \mathcal{H}_{\mathrm{DD}}(t) + \mathcal{H}_{\mathrm{CS}}(t) + \mathcal{H}_{\mathrm{RF}}(t) + \mathcal{H}_{\mathrm{E}}(t). \tag{1}$$

The time dependence of $\mathcal{H}_{\mathrm{DD}}$ and $\mathcal{H}_{\mathrm{CS}}$ originates from MAS, and that of $\mathcal{H}_{\mathrm{RF}}$ and $\mathcal{H}_{\mathrm{E}}$ from the specific RF irradiation field. When we assume that the RF irradiation, including the pulse errors, is periodic with a characteristic time constant $t_{\mathrm{c}} = 2\pi/\omega_{\mathrm{c}}$ and the rotor frequency is ω_r, the different terms can be expanded in a Fourier series as:

$$\mathcal{H}_{\mathrm{DD}}(t) = \sum_{i>j}\sum_{n=-2}^{2} \omega_{ij} G_{n,ij} \mathrm{e}^{\mathrm{i}n\omega_r t}\sqrt{6} T^{(2)}_{0,ij}, \tag{2a}$$

$$\mathcal{H}_{\mathrm{CS}}(t) = \sum_{j}\left\{ \Delta\omega_{0j} T^{(1)}_{0,j} + \sum_{n=-2}^{2} \omega_j g_{n,j} \mathrm{e}^{\mathrm{i}n\omega_r t} T^{(1)}_{0,j} \right\}, \tag{2b}$$

$$\mathcal{H}_{\mathrm{RF}}(t) = \omega_1 \sum_j \sum_k \left\{ a_{1,k} T^{(1)}_{+1,j} + a_{-1,k} T^{(1)}_{-1,j} \right\} \mathrm{e}^{\mathrm{i}k\omega_c t}, \tag{2c}$$

$$\mathcal{H}_{\mathrm{E}}(t) = \omega_1 \sum_j \sum_k \left\{ b_{1,k} T^{(1)}_{+1,j} + b_{-1,k} T^{(1)}_{-1,j} \right\} \mathrm{e}^{\mathrm{i}k\omega_c t}. \tag{2d}$$

Here, $\omega_{ij} = \mu_0\gamma^2\hbar/4\pi r^3_{ij}$ are the dipolar interaction frequencies, $\Delta\omega_{0j}$ are the isotropic chemical-shift values plus some constant offset values and ω_j are the CSA frequencies. $G_{n,ij}$ and $g_{n,j}$ are complex geometric factors depending on the initial directions of the distance vectors r_{ij} between spins i and j and the CSA tensor orientations [21]. The relative Fourier coefficients $a_{\pm1,k}$ and $b_{\pm1,k}$ are the parameters describing, respectively, the ideal part and the imperfections of the RF irradiation field experienced by the spins in the rotating frame. $\mathcal{H}_{\mathrm{RF}}(t)$ represents one of the homonuclear dipolar decoupling schemes that can be used to narrow the proton spectra of solids. ω_1 is the RF nutation frequency.

In the PMLG*n* [12], BLEW12 [22], and DUMBO [16] schemes the RF phases change from pulse to pulse but the RF amplitude stays constant, while in the windowed sequences like *w*PMLG*n* [17], MREV8 [23], BR24 [24], and MSHOT3 [25,26] the RF trains vary in phase and amplitude due to the presence of observation windows in between the RF pulse trains where $\omega_1 = 0$.

The common way to evaluate the spin response to a periodic set of RF pulses under MAS is to transform the Hamiltonian to the RF interaction frame. The transformation of a Hamiltonian to the RF interaction frame is then given by

$$\tilde{\mathcal{H}}(t) = U^{-1}_{\mathrm{RF}}(t)\mathcal{H}(t)U_{\mathrm{RF}}(t). \tag{3}$$

The transformation operator U_{RF} is given by

$$U_{\mathrm{RF}}(t_c) = \mathcal{T}\ \exp\left\{ \mathrm{i}\int_0^{t_c} H_{\mathrm{RF}}(t)\mathrm{d}t \right\} = 1. \tag{4}$$

If the irreducible tensor components $T^{(l)}_m$, $(m = -l, ..., l)$ transform like

$$U_{\mathrm{RF}}^{-1}(t)T_m^{(l)}U_{\mathrm{RF}}(t)=\sum_{m'}\sum_{k}d_{m,m',k}^{(l)}T_{m'}^{(l)}\mathrm{e}^{\mathrm{i}k\omega_c t} \tag{5}$$

the interaction Hamiltonian terms become

$$\tilde{\mathcal{H}}_{\mathrm{DD}}(t)=\sum_{i>j}\sum_{n,k}\sum_{m}\omega_{ij}G_{n,ij}d_{0,m,k}^{(2)}\sqrt{6}T_{m,ij}^{(2)}\mathrm{e}^{\mathrm{i}n\omega_r t}\mathrm{e}^{\mathrm{i}k\omega_c t},$$

$$\tilde{\mathcal{H}}_{\mathrm{CS}}(t)=\sum_{j}\sum_{k}\sum_{m}d_{0,m,k}^{(1)}\times\left\{\Delta\omega_j T_{m,j}^{(1)}+\sum_{n}\omega_j g_{n,j}T_{m,j}^{(1)}\mathrm{e}^{\mathrm{i}n\omega_r t}\right\}\mathrm{e}^{\mathrm{i}k\omega_c t},$$

$$\tilde{\mathcal{H}}_{\mathrm{E}}(t)=\omega_1\sum_{j}\sum_{k}\sum_{m}\left\{\delta_{m,k}T_{m,j}^{(1)}\right\}\mathrm{e}^{\mathrm{i}k\omega_c t}, \tag{6}$$

where

$$\delta_{m,k}=\sum_{k'}\left\{b_{+1,k'}d_{+1,m,(k-k')}^{(1)}+b_{-1,k'}d_{-1,m,(k-k')}^{(1)}\right\} \tag{7}$$

are the relative Fourier components of the RF imperfections transformed to the ideal RF interaction frame. The error terms could be added to the isotropic chemical-shift terms and considered as isotropic chemical-shift error terms, $d_{0,m,k}^{(1)}\Delta\omega_i\rightarrow(d_{0,m,k}^{(1)}\ \Delta\omega_i+\omega_1\delta_{m,k})$. With this consideration, it can thus be expected that the decoupled chemical-shift spectrum will be dependent on the magnitude of the RF imperfections. Both DD and CSA interaction terms become periodic with two independent time constants after the transformation to the RF interaction frame.

To proceed let us assume that the ideal decoupling sequence eliminates the zero-order effective interaction Hamiltonian $\tilde{\mathcal{H}}_{\mathrm{DD,eff}}^{(0)}$. Utilising the bimodal Floquet theory approach, and assuming that the characteristic frequencies ω_c and ω_r do not satisfy the condition $\nu\omega_r=\kappa\omega_c$ for integers ν and κ with $\nu/\kappa<2$ and $\nu/\kappa=3,4$, this effective Hamiltonian is zero as long as the dipolar coefficients in Eq. (6) are smaller than their corresponding Floquet energy differences [5,17]:

$$\left|\omega_{ij}G_{n,ij}d_{m-k}^{(2)}\right|<<|n\omega_r-k\omega_c|. \tag{8}$$

In this case the total zero-order effective Hamiltonian contains the scaled isotropic chemical-shift terms plus the correction terms

$$\tilde{\mathcal{H}}_{\mathrm{eff}}^{(0)}=\sum_{j}\Delta\omega_{0j}\left\{d_{0,0,0}^{(1)}T_{0,j}^{(1)}+d_{0,1,0}^{(1)}T_{1,j}^{(1)}+d_{0,-1,0}^{(1)}T_{-1,j}^{(1)}\right\} \tag{9}$$

$$+\omega_1\left\{\delta_{0,0}T_{0,j}^{(1)}+\delta_{1,0}T_{1,j}^{(1)}+\delta_{-1,0}T_{-1,j}^{(1)}\right\}. \tag{10}$$

The two parts of this corrected chemical-shift Hamiltonian are the "ideally" scaled isotropic chemical-shift Hamiltonian plus a constant correction Hamiltonian. Both can be represented in terms of a linear angular momentum component, pointing in some directions $\bar{s}$, and $\bar{c}$ with polar angles $(\theta_{s,c},\phi_{s,c})$ in the rotating frame:

$$\tilde{\mathcal{H}}_{\mathrm{eff}}^{(0)}=\sum_{j}s\Delta\omega_{0j}I_{\bar{s},j}+c\omega_1 I_{\bar{c}}. \tag{11}$$

The "ideal" scale factor is defined by the Fourier coefficients of the specific decoupling sequence

$$s=\left\{|d_{0,0,0}|^2+|d_{0,+1,0}|^2+|d_{0,-1,0}|^2\right\}^{1/2} \tag{12}$$

and the effective chemical-shift direction by

$$\tan\theta_s=\frac{\sqrt{\left(d_{0,+1,0}^{(1)}\right)^2+\left(d_{0,-1,0}^{(1)}\right)^2}}{d_{0,0,0}^{(1)}},$$

$$\tan\phi_s=\mathrm{i}\frac{d_{0,+1,0}^{(1)}-d_{0,-1,0}^{(1)}}{d_{0,+1,0}^{(1)}+d_{0,-1,0}^{(1)}}. \tag{13}$$

These angles and the scale factor s are independent of the magnitudes and signs of the offset values $\Delta\omega_{0j}$. The constant RF correction term, independent of $\Delta\omega_{0j}$, is defined in a similar fashion by

$$c=\left\{|\delta_{0,0}|^2+|\delta_{+1,0}|^2+|\delta_{-1,0}|^2\right\}^{1/2} \tag{14}$$

and

$$\tan\theta_c=\frac{\sqrt{\left(\delta_{+1,0}^{(1)}\right)^2+\left(\delta_{-1,0}^{(1)}\right)^2}}{\delta_{0,0}^{(1)}},$$

$$\tan\phi_c=\mathrm{i}\frac{\delta_{+1,0}^{(1)}-\delta_{-1,0}^{(1)}}{\delta_{+1,0}^{(1)}+\delta_{-1,0}^{(1)}}. \tag{15}$$

Since the value of the c-coefficient is determined by the RF imperfections it is almost always impossible to predict its value. Thus we must conclude that the corrected isotropic chemical-shift Hamiltonian terms can be characterised by effective off-resonance fields that are composed of the ideal scaled chemical-shift fields plus a correction field that is constant and pointing in some arbitrary direction. When, to zero-order, the line positions in the decoupled proton spectrum are defined by Eq. (11), the vector sum of the two fields determines their overall off-resonance value

$$\Delta\omega_j=\pm\sqrt{\left(s\Delta\omega_{0j}\right)^2+\left(c\omega_1\right)^2}, \tag{16}$$

where the $\pm$ is chosen to keep the signs of the offset values $\Delta\omega_{0j}$ and experimentally observed off-resonance values $\Delta\omega_j$ equal. The polar angles $(\theta_j,\ \phi_j)$ of the sum of the fields are chosen according to this rule. Thus at very far off-resonance we can assume that $\theta_j\simeq\theta_s$ and $\phi_j\simeq\phi_s$. These direction angles can vary strongly for small $\Delta\omega_{0j}$ values. This is demonstrated for some arbitrary correction field in Fig. 1.

Before discussing the practical aspects of the influence of the RF imperfections on proton spectra, we should consider the higher-order terms of the effective Hamiltonian. Following the van Vleck perturbation approach

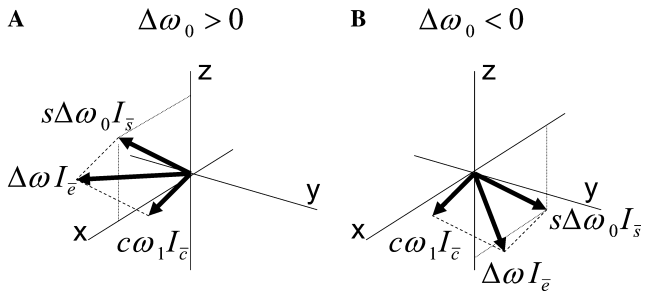

Fig. 1. A schematic of the effective field in the rotating frame created by the sum of the two fields: field due to the effective isotropic chemical shift and offset values ($s\Delta\omega_0 I_{\bar{s}}$), and the field induced by the RF pulse imperfections ($c\omega_1 I_{\bar{c}}$). Two cases are shown: (A) positive $\Delta\omega_0$ value and (B) negative $\Delta\omega_0$ value.

in the bimodal Floquet description of the Floquet space representation of the interaction Hamiltonian in Eq. (6), we have shown that for protons at high spinning frequencies the most important higher-order effective Hamiltonian term is the first-order dipole–dipole effective Hamiltonian $\tilde{\mathcal{H}}^{(1)}_{\mathrm{DD}}$ and not the mixed chemical shift-dipolar first-order Hamiltonian terms [5]. In the same way we can expect that the error terms in the interaction Hamiltonian will have a very minor contribution to mixed error-dipolar first-order terms. Furthermore, we can expect that the error terms, as long as they are small ($\omega_1\delta_{m,k} << \Delta\omega_{0j} d^{(1)}_{0,m,k}$), will shift the lines in the spectrum as predicted above, but will not cause any significant broadening.

3. Numerical simulations

To verify these theoretical predictions we employed spectral simulations using SPINEVOULTION [26] programme. The *w*PMLG5 decoupling sequence was used and phase and amplitude imperfections were introduced in the perfect irradiation scheme. To find some typical example of a possible RF distortion an experimental high power *w*PMLG5 pulse sequence, entering a tuned MAS-probe of the DSX 300 MHz spectrometer, was detected by an RF directional coupler, and displayed on a digital oscilloscope. The result of this measurement is shown in Fig. 2A. The individual pulses of 1.73 μs are distorted in amplitude and phase at least for a time period of about 100 ns at their start. The exact imperfections appearing in the RF field at the place of the sample are of course unknown. The *w*PMLG5* pulse sequence used in the simulations is shown in Fig. 2B. The RF train resembles the experimentally achieved pulse profile, the * denoting a sequence with imperfections. In the simulations the RF amplitude was

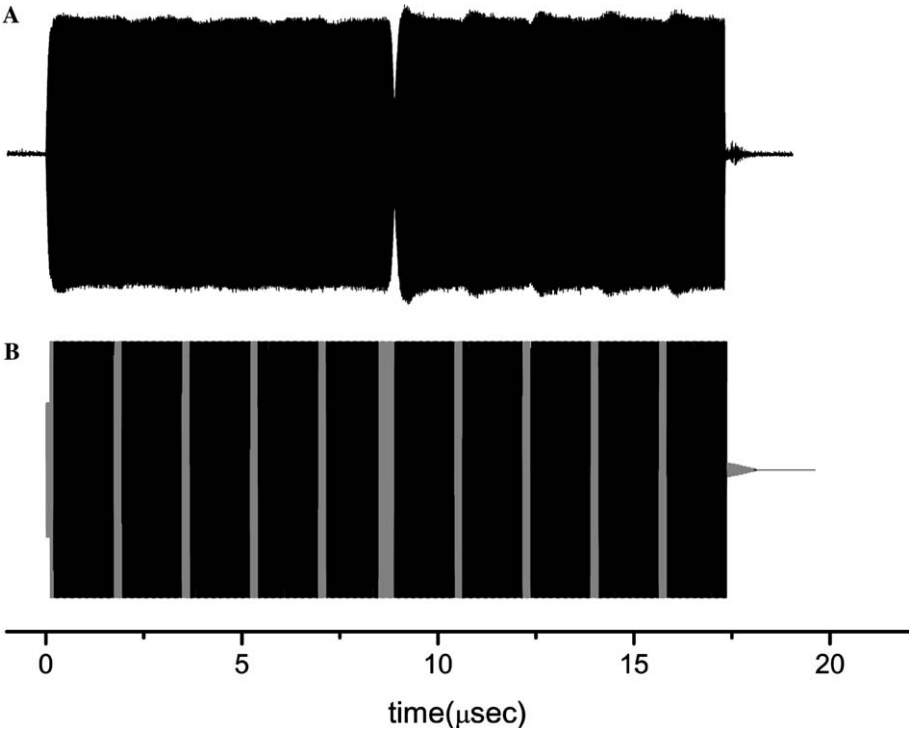

Fig. 2. (A) The RF profile of the 10 RF pulses composing the *w*PMLG5 pulse unit, generated on a DSX-300 spectrometer, measured by a linear power detector and displayed on a digital oscilloscope. (B) The pulse unit used for the *w*PMLG5* simulations (shown in Figs. 3–5). The black pulses are constant amplitude RF irradiations with phases chosen according to the ideal *w*PMLG scheme. The gray areas represent RF irradiations with phases that are equal to the average of the phases of the irradiations before and after these short pulses. The actual values of the RF intensity and phases are discussed in the text.

assumed to be 95 kHz and the total irradiation period, which is the length of a *w*PMLG5 unit, was 17.3 μs. The RF amplitude was kept constant during this period except during the first 100 ns and during an extension of the sequence of 750 ns. The amplitudes of the RF pulses was 50 kHz during the initial 100 ns of the RF profile. The amplitudes of the RF pulses during the last 750 ns of the RF profile were 5.1, 4.5, 3.8, 3.2, 2.6, 1.9, and 1.3 kHz for a duration of 100 ns each and 0.6 kHz for the last duration of 50 ns. The ideal infinitesimal phase switches between the pulses were replaced by 200 ns irradiation periods with phases equal to the average values of the previous and following pulses. In addition, during the 300 ns duration in the middle of the RF profile, the phase value was equal to the value of the previous pulse phase. The total duration of each *w*PMLG5 unit, with a detection window of 3.4 μs, was not modified and the characteristic RF frequency of the *w*PMLG5 sequences was $\omega_c/2\pi = 1/\tau_c = 48.31$ kHz.

Simulations of single-spin spectra were performed as a function of its isotropic chemical shift value $\Delta\nu_0 = \Delta\omega_0/2\pi$, employing *w*PMLG5*. Following a 90° excitation pulse and *w*PMLG5* irradiation the magnetisation of the spins precesses around an effective field in the rotating frame, with a Hamiltonian of the form $(s\Delta\nu_0 I_{\bar{s}} + c\nu_1 I_{\bar{c}})$, the effective chemical-shift field pointing in the $\bar{s}$ direction plus an additional field pointing in the $\bar{c}$ direction. Here, $\nu_1 = \omega_1/2\pi$. The direction of the total effective field can be described by polar angles $\{\theta, \phi\}$ and an amplitude corresponding to the detected off-resonance value as in Eq. (16) can be estimated as $\Delta\nu = \Delta\omega/2\pi$. The values of the two polar angles and the observed off-resonance as a function of $\Delta\nu_0$ were measured and the results are plotted in Fig. 3 for both *w*PMLG5* and ideal *w*PMLG5. As expected, for large chemical shifts ($\Delta\nu_0 >> c\nu_1$) the total field direction is mainly determined by the effective chemical-shift direction and hence, it should be close to the ideal *w*PMLG5 effective field direction, which is near the magic-angle direction with $\theta_s = 54.7°$ and, for our pulse sequence, $\phi_s = 0$. When the chemical shifts are small, the effective field direction is strongly influenced by the imperfections. At on-resonance, $\Delta\nu_0 = 0$, the effective field direction is solely determined by the imperfection term $c\nu_1 I_{\bar{c}}$. From Fig. 3 it can be deduced that for our distorted *w*PMLG5* sequence this direction almost points in the $+x$ direction: $\{\theta_c = 95.6°, \phi_c = 15.3°\}$.

There is a region at negative $\Delta\nu_0$ values around −4.5 kHz, where the vector sum of the two fields results in an effective field direction almost parallel to z. Hence, around this value the magnetisation will precess about around the z direction resulting in a single-peak spectrum. The magnetisation trajectories, monitored synchronously, and the direction of their effective fields are shown in Fig. 4 for three cases: for *w*PMLG5* irradiation with $\Delta\nu_0 = +5$ kHz and $\Delta\nu_0 = -5$ kHz and for an ideal PMLG9 scheme with $\Delta\nu_0 = -5$ kHz. It is illustrated in this figure that in the case of positive $\Delta\nu_0$, as well as in the ideal PMLG case, the projection of the magnetisation trajectory on to the $x-y$ plane generates an observable that corresponds to an elliptical pathway, and, hence, after Fourier transformation an image peak will appear in the spectrum. On the contrary, for *w*PMLG5*, around $\Delta\nu_0 \simeq -5$ kHz the rotation axis is close to the z-direction ($\theta \simeq 0^0$) and the $x-y$ magnetisation trajectory is close to a circle, and hence the image peak is very small. We chose PMLG9 for comparison as this is the closest to FSLG in the ideal case with $\theta = 54.7°$.

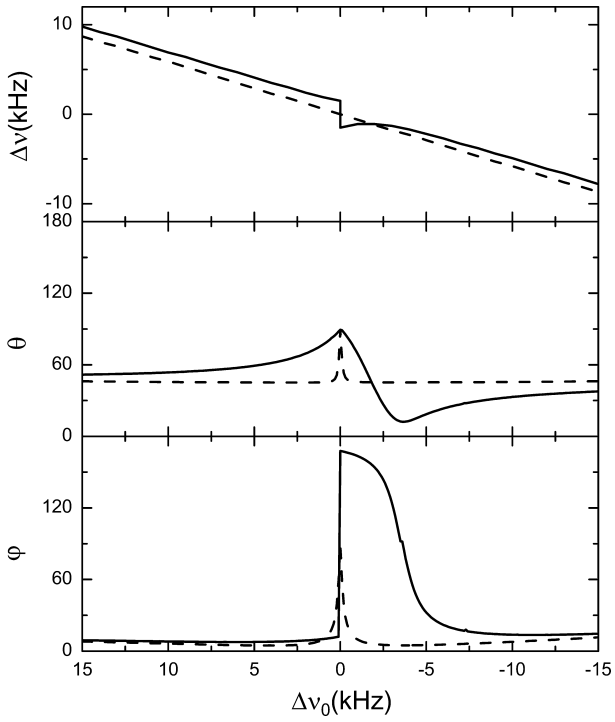

Fig. 3. Single-spin simulations of the synchronously detected magnetisation pathways during *w*PMLG5* irradiation (continuous lines), as shown in Fig. 2B, enable the determination of the effective rotation frequency $\Delta\nu$ and the direction angles (θ, ϕ) of the norm to the plane of rotation. In this figure $\Delta\nu$, θ, and ϕ are plotted as a function of the offset value $\Delta\nu_0$. Also shown are the respective plot for ideal *w*PMLG5 (dashed lines).

The off-resonance measured in the spectrum, $\Delta\nu$, corresponds to the magnitude of the effective field. Hence, at large chemical shifts the observed off-resonance value $\Delta\nu$ is shifted from $s\Delta\nu_0$ by the same constant value, while for small $\Delta\nu_0$ values the effective scale factor $s(\Delta\nu_0) = \partial\Delta\nu/\partial\Delta\nu_0$ varies. In our simulations this scale factor is zero around $\Delta\nu_0 \simeq -2$ kHz. This leads to spectral distortions in multi-spin spectra when s is not a constant. To verify the decoupling efficiency of the *w*PMLG5* sequence proton spectra were simulated for a model system containing five protons, as shown in Fig. 5. The relative positions and the chemical shifts of

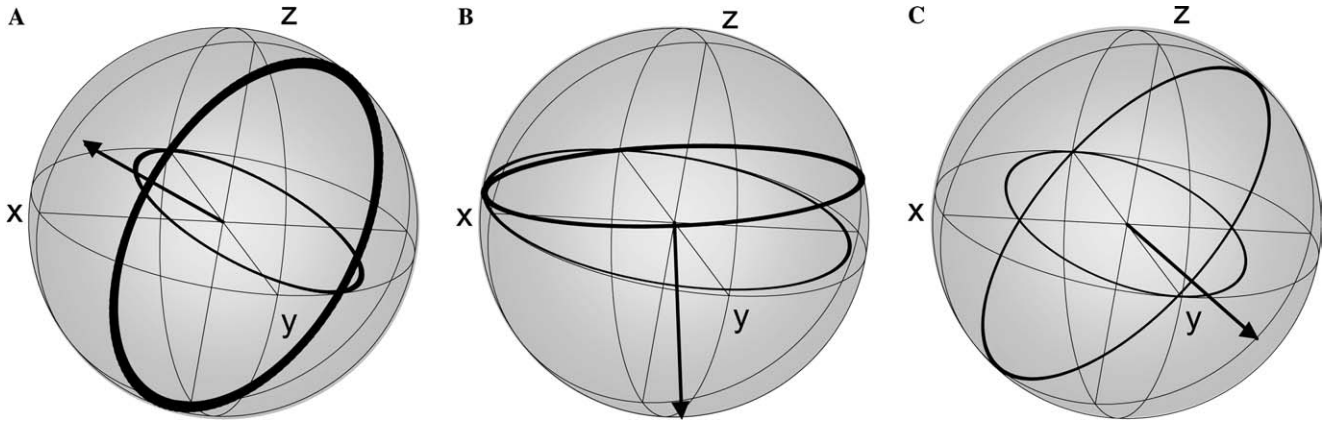

Fig. 4. Calculated magnetisation trajectories in the rotating frame starting from the $-y$ axis during a *w*PMLG5* irradiation shown for (A) $\Delta\nu_0 = +5\,\text{kHz}$ and (B) for $\Delta\nu_0 = -5\,\text{kHz}$. Response for ideal PMLG9 is shown in (C) for $\Delta\nu_0 = -5\,\text{kHz}$. In addition to the synchronously detected magnetisation pathways their projections onto the $x - y$ plane are also shown. The unit vectors in the three spheres are pointing in the direction of the norm to the planes of rotation of the magnetisations.

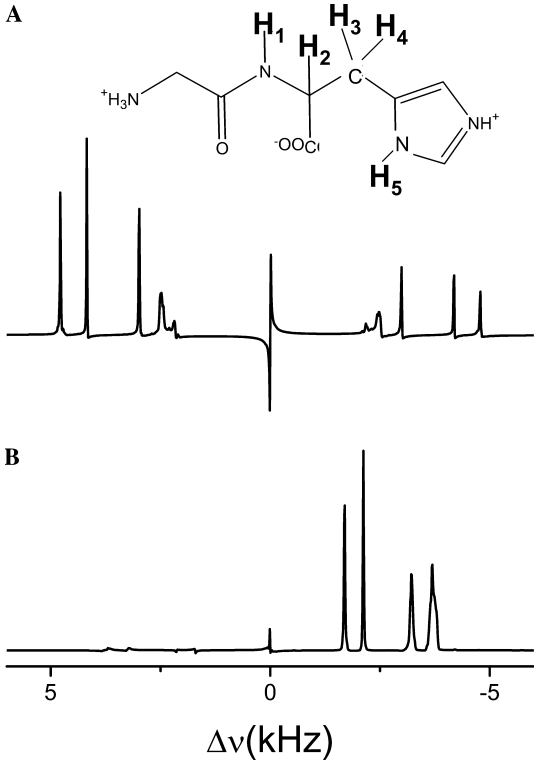

Fig. 5. Simulated *w*PMLG5* spectra of the five coupled protons of the model compound shown on the top. The proton Larmor frequency was assumed to be 600 MHz and the spinning frequency was 13.75 kHz. The chemical-shift and offset parameters of the protons are summarised in Table 1.

these protons were chosen as shown in Table 1. No CSA and *J*-coupling interactions were taken into account during the simulations. The spinning frequency used was $\omega_r/2\pi = 13.753\,\text{kHz}$, which corresponds to $\omega_c = 3.5\omega_r$.

In Fig. 5 two spectra of the model compound are shown that were simulated assuming a proton Larmor frequency of 600 MHz: (a) with positive offset $\Delta\nu_{0i}$, and (b) negative offset $\Delta\nu_{0i}$ values as summarised in Table 1. When the positive offsets are used relatively large image peaks appear, indicating that the effective fields of the spins in the rotating frame do not point in the $\pm z$ direction. On the contrary, at negative offset values, the image peaks are very small and almost not noticeable. These results are in agreement with the simple single-spin calculation results discussed earlier. Notice also the improved resolution at the negative offset region that is in particular obvious for the CH_2 line. This spectral resolution is obtained in spite of the slightly varying scale factor. The reason for this line narrowing could be a result of the truncation of the first-order effective dipolar Hamiltonian with respect to the modified zero-order effective chemical shift Hamiltonian. Further investigation of this effect will be necessary in order to take full advantage of the *w*PMLG*n** schemes.

4. Experimental

*w*PMLG5 experiments were performed on a Bruker DSX spectrometer operating at 300 MHz and on a Varian Infinity Plus spectrometer, operating at 600 MHz. Samples of L-histidine·HCl·H_2O, L-tyrosine and monoethyl fumarate were used at both the magnetic fields. In addition, a sample of DL-glycine was used at the 600 MHz field. The repetition delay was 5 s for L-histidine, monoethyl fumarate, and glycine and 10 s for L-tyrosine. The phase increments in the two sequential parts of each *w*PMLG5 cycle were $\Delta\phi = \pm 41.6°$ starting with 20.78° for positive increments and 7.02° for negative increments. In both the spectrometers the individual PMLG pulse width Δt, and the RF power ω_1, were fine adjusted for the best resolution. Single $\pi/2$ pre-pulses with phases $x, y, -x, -y$ were applied before the data

Table 1
The proton coordinates in an arbitrary molecular reference frame and chemical-shift values of the model compound shown in Fig. 5, together with positive and negative offset values

	x (Å)	y (Å)	z (Å)	δ (ppm)	$\Delta\nu_{0i} > 0$ (kHz)	$\Delta\nu_{0i} < 0$ (kHz)
$H^{(1)}$	−4.58	12.57	7.26	8.3	4.98	−4.52
$H^{(2)}$	−2.26	11.71	6.08	4.6	2.76	−6.74
$H^{(3)}$	−4.42	9.86	6.73	3.12	1.872	−7.628
$H^{(4)}$	−3.24	9.47	5.93	3.12	1.872	−7.628
$H^{(5)}$	−3.81	7.87	8.31	10.1	6.06	−3.44

acquisition with detection phases of 0°, 90°, 180°, and 270°, respectively. On the DSX-300 spectrometer a 4 mm CRAMPS probe was used and the acquisition window t_w was of a length 3.4 μs. A list of fixed RF phases generating the PMLG5 profile was employed with $\Delta t = 1.74$ μs. The spinning frequencies used were 10.00, 14.286, and 14.286 kHz for L-histidine, monoethyl fumarate and L-tyrosine, respectively. All the samples were confined by spacers to the center of the rotors in order to improve the RF inhomogeneity: the L-histidine sample to 0.5 mm, monoethyl fumarate to 1.5 mm and L-tyrosine to 1 mm. The synchronously detected free induction decay signals were collected at the end of the detection windows and 1 K points were acquired.

On the Infinity Plus 600 spectrometer a 4 mm standard double resonance probe was used with $\Delta t = 1.7$ μs. The acquisition window length was optimised separately for each sample to obtain the best resolution and was equal to 4.6, 6.3, 5.3, and 6.1 μs for L-histidine·HCl·H_2O, monoethyl fumarate, glycine, and L-tyrosine, respectively. Small delays of 0.1 μs were inserted between all the PMLG pulses to improve the RF performance. The samples were confined to the center of the rotors: L-histidine·HCl·H_2O to 1.5 mm, monoethyl fumarate to 1.5 mm, tyrosine to 1 mm, and glycine to 2 mm. The spinning frequency was 10 kHz in all the experiments on the Infinity Plus 600 spectrometer. The signals were detected synchronously in the windows of the *w*PMLG5 sequence and 256 points were acquired.

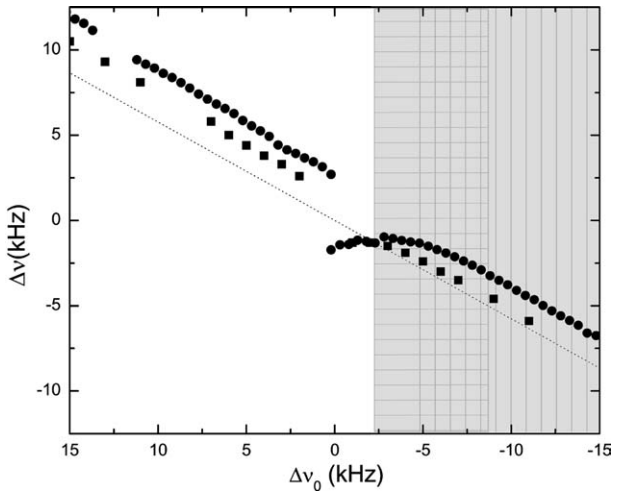

Fig. 6. Experimentally observed position of the NH_3 proton line of glycine and the carboxyl proton line of monoethyl fumarate, $\Delta\nu$, as a function of their off-resonance values, $\Delta\nu_0$, respectively, measured on a Varian Infinity Plus 600 spectrometer (filled circles) and on a Bruker DSX-300 spectrometer (filled squares). One scan was used for the experiments on glycine and 4 scans with CYCLOPS phase cycling for the experiments on monoethyl fumarate. The dotted line shows the line $\Delta\nu = s\Delta\nu_0$ with a constant scale factor of 0.577. The optimal offset regions to be used in the experiments are indicated by horizontal, for the DSX-300, and vertical, for the Infinity Plus 600 spectrometer, striped gray areas. In these regions the experimental scale factor defined in Eq. (16) are larger than 0.45, and in part of these regions the effective rotation axis point about in the direction of the z-axis.

5. Results

To measure the scale factor as a function of the offset value $\Delta\nu_0$ *w*PMLG5* experiments were performed on the glycine sample at 600 MHz and on the monoethyl fumarate sample at 300 MHz. In the former case the position $\Delta\nu$ of the NH_3 line was monitored and in the latter the position of the carboxyl line. The results of these experiments are shown in Fig. 6. The observed values of $\Delta\nu$ show a similar dependence as obtained for the simulations using the *w*PMLG5* sequence of Fig. 3. It is evident that both the spectrometers result in an asymmetric response for $\pm\Delta\nu_0$ with similar profiles as in Fig. 3. It follows that the fields corresponding to the RF error terms $c\omega_1 I_{\bar{c}}$ in the effective Hamiltonian point about in the same direction close to the $x - y$ plane. The scale factors of both experiments away from the on-resonance condition are about 0.64, while close to resonance they approach zero and even become negative. The figure indicates that the Infinity Plus 600 generates a larger shift $(\Delta\nu - s\Delta\nu_0)$ than the DSX-300 spectrometer. As a result a proton spectrum of a spectral width of about 15 ppm must be collected such that -5 kHz $< \Delta\nu_{0i} < -15$ and -2.5 kHz $< \Delta\nu_{0i} < -8$ kHz for the 600 and 300 MHz spectrometers, respectively. These optimal ranges are indicated in the figure. The comparison between these results and the simulated results in Fig. 3A shows a strong resemblance for the results from the 300 MHz machine. We can therefore expect that the tilt angles θ in the detection range behave also similarly and are smaller than 35°. Similar conclusions about the data from the the Infinity Plus 600 MHz are possible, but we

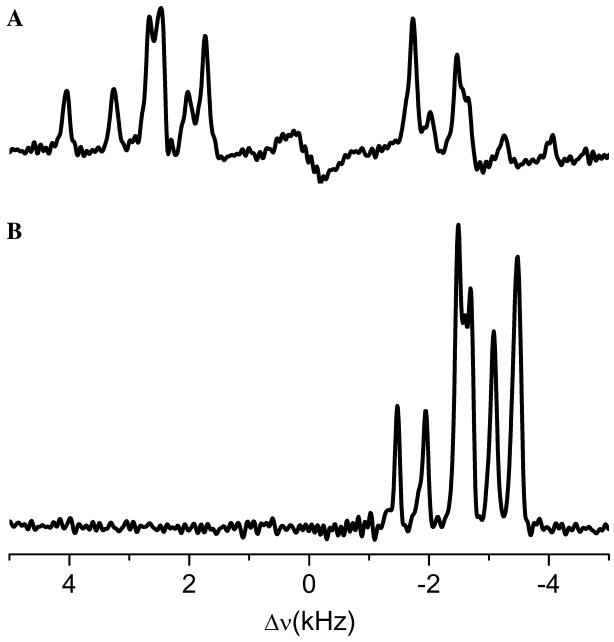

Fig. 7. L-Histidine·H_2O·HCl spectra measured at 300 MHz on a Bruker DSX-300 spectrometer at a spinning frequency of 10 kHz with (A) the positive offsets $\Delta\nu_{0i} > 0$ and (B) negative offsets $\Delta\nu_{0i} < 0$. Four-phase CYCLOPS phase cycling was used to obtain these spectra.

did not try to generate RF imperfections in the ideal *w*PMLG5 scheme that gave the 600 MHz results as in Fig. 6.

To verify further the experimental behaviour as a function of the resonance offset, *w*PMLG5 measurements at positive and negative offsets were performed on a L-histidine sample at 300 MHz, the resulting two spectra shown in Fig. 7. For negative $\Delta\nu_{0j}$'s the spectrum does not show any image peaks or zero-frequency lines. The scale factor of the positive $\Delta\nu_0$ spectrum is slightly larger than for $\Delta\nu_0 < 0$, and at the negative side the scale factor is not constant over the whole spectrum. For an accurate line position measurement on ppm scale a calibration curve must be generated to correlate the observed line positions with their actual chemical-shift values. Fig. 8 shows proton *w*PMLG5* spectra of three samples: monoethyl fumarate, L-histidine·HCl·H_2O and L-tyrosine, measured at 300 and 600 MHz magnetic fields. All spectra were collected with $\Delta\nu_0 < 0$ and do not show image peaks. The improved spectral resolutions are a result of the use of the confinement of the samples in the middle of the spinners, and the fact that the RF imperfections cause additional line narrowing as discussed above. The zero-frequency lines in the

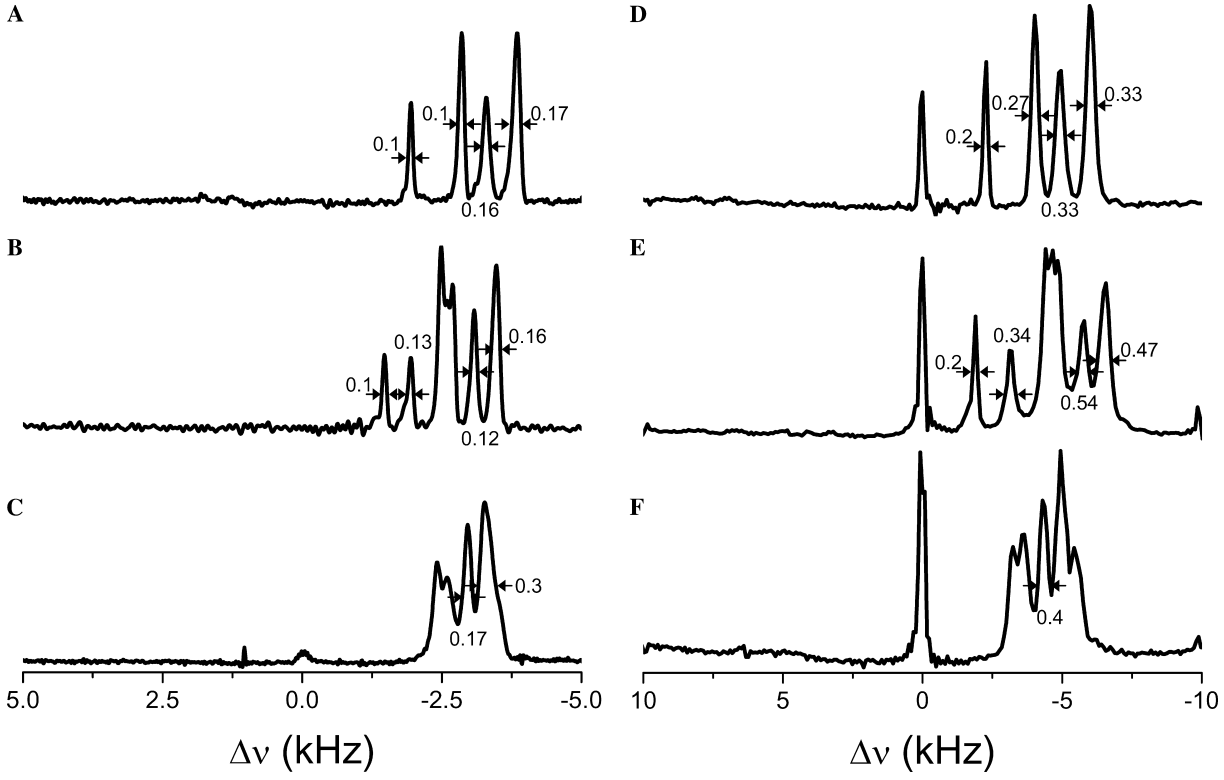

Fig. 8. Experimental *w*PMLG5 spectra of (A and D) monoethyl fumarate, (B and E) L-histidine·HCl·H_2O and (C and F) L-tyrosine measured on a Bruker DSC-300 spectrometer (A–C) and Varian Infinity Plus 600 spectrometer (D–F) with $\omega_r/2\pi = 10$ kHz and four steps CYCLOPS phase cycling. The number of transients was 8 in (A and B), 16 in (C), 4 in (D), 60 in (E), and 20 in (F). Certain representative line widths are indicated in the spectra in kHz.

600 MHz spectra may be eliminated by adjusting the phase of the 90° pulse so that there is no component of the magnetisation vector along the direction of the effective field during spin evolution.

6. Conclusions

The modifications in the spin evolution due to the RF imperfections during *w*PMLG5 decoupling experiments were studied and their influence on the decoupled proton spectra were analysed. The actual distortions of the experimental RF pulse shapes and phases depend on the hardware performance of the spectrometer, but they will always generate some additional effective field in the rotating frame that will influence the trajectories of the spin magnetisations. Because it will be very hard to totally eliminate these effects it will be necessary to deal with the imperfection induced effects and to adjust the experimental set-up of the decoupling experiments accordingly. In this publication it was shown that we can benefit from the imperfections in terms of spectral sensitivity and resolution. Experiments on two different spectrometers demonstrated similar effect. With the proper experimental parameters the isotropic chemical shift spin evolution during *w*PMLG5* can be represented after a single 90° excitation pulse with CYCLOPS phase cycling in the rotating frame as magnetisation vectors rotating close to the $x-y$ plane. This enables simple phase cycling schemes during one-dimensional data acquisition, generating spectra without frequency images. Due to the imperfections the scale factors of the experiments are not constant over the spectra, a fact that must be realised during chemical-shift data analysis. Finally, we should mention that an important source of line broadening observed in high-resolution proton spectra is the RF inhomogeneity across the samples. This effect was not discussed here but needs much attention when research efforts are pointing towards further resolution enhancement.

Acknowledgment

The authors thank the Minerva Science Foundation for financial support.

References

[1] B.-J. van Rossum, H. Forster, H.J.M. De Groot, High-field and high-speed CP-MAS ^{13}C heteronulcear dipolar correlation spectroscopy of solids with frequency-switched Lee-Goldburg homonuclear decoupling, J. Magn. Reson. 124 (1997) 516–519.

[2] A. Lesage, D. Sakellariou, S. Steuernagel, L. Emsley, Carbon–proton chemical shift correlation in solid-state NMR by through-bond multiple-quantum spectroscopy, J. Am. Chem. Soc. 120 (1998) 13194–13201.

[3] B.-J. van Rossum, F. Castellani, K. Rehbein, J. Pauli, H. Oschkinat, Assignment of the nonexchanging protons of the α-spectrin SH3 domain by two- and three-dimensional ^{1}H–^{13}C solid-state magic-angle spinning NMR and comparison of solution and solid-state proton chemical shifts, Chem. BioChem. Eng. Q 2 (2001) 906–914.

[4] A.F.L. Creemers, S. Kiihne, P.H.M. Bovee-Geurts, W.J. DeGrip, J. Lugtenburg, H.J.M. De Groot, ^{1}H and ^{13}C MAS NMR evidence for pronounced ligand–protein interactions involving the inone ring of the retinylidene chromophore in rhodopsin, Proc. Natl. Acad. Sci. USA 99 (2002) 9101–9106.

[5] E. Vinogradov, P.K. Madhu, S. Vega, Strategies for high-resolution proton spectroscopy in the NMR of solid-state, Topics in Current Chemistry, Springer, Berlin, 2004, in press.

[6] M. Lee, W. Goldburg, Nuclear magnetic resonance line narrowing by rotating rf fields, Phys. Rev. A 140 (1965) 1261–1271.

[7] J.S. Waugh, L.M. Huber, U. Haeberlen, Approach to high resolution NMR in solids, Phys. Rev. Lett. 20 (1968) 180–183.

[8] U. Haeberlen, High resolution NMR in solids: selective averaging, Adv. Magn. Reson. 1 (1976) 1–190.

[9] R.G. Pembleton, L.M. Ryan, B.C. Gerstein, NMR probe for combined homonuclear multiple pulse decoupling and magic angle spinning, Rev. Sci. Instrum. 48 (1977) 1286–1289.

[10] C.E. Bronnimann, B.L. Hawkins, M. Zhang, G.E. Maciel, Combined rotation and multiple pulse spectrosocpy as an analytical proton nuclear magnetic resonance technique for solids, Anal. Chem. 60 (1988) 1743–1750.

[11] M.H. Levitt, A.C. Kolbert, A. Bielecki, D.J. Ruben, Proton line-narrowing in solids with frequency-switched pulse sequences, Solid State Nucl. Magn. Reson. 2 (1993) 151–163.

[12] E. Vinogradov, P.K. Madhu, S. Vega, High-resolution proton solid-state NMR spectroscopy by phase-modulated Lee-Goldburg experiment, Chem. Phys. Lett. 314 (1999) 443–450.

[13] E. Vinogradov, P.K. Madhu, S. Vega, A bimodal Floquet analysis of phase modulated Lee-Goldburg high resolution proton magic angle spinning NMR experiments, Chem. Phys. Lett. 329 (2000) 207–214.

[14] E. Vinogradov, P.K. Madhu, S. Vega, Phase modulated Lee-Goldburg magic angle spinning proton nuclear magnetic resonance experiments in the solid state: a bimodal Floquet theoretical treatment, J. Chem. Phys. 115 (2001) 8983–9000.

[15] P.K. Madhu, X. Zhao, M.H. Levitt, High-resolution ^{1}H NMR in the solid state using symmetry-based pulse sequences, Chem. Phys. Lett. 346 (2001) 142–148.

[16] A. Lesage, D. Sakellariou, S. Hediger, B. Elèna, P. Charmont, S. Steuernagel, L. Emsley, Experimental aspects of proton NMR spectroscopy in solids using phase-modulated homonuclear dipolar decoupling, J. Magn. Reson. 163 (2003) 105–113.

[17] E. Vinogradov, P.K. Madhu, S. Vega, Proton spectroscopy in solid state nuclear magnetic resonance with windowed phase modulated Lee-Goldburg decoupling sequences, Chem. Phys. Lett. 354 (2002) 193–202.

[18] M. Mehring, J.S. Waugh, Phase transients in pulsed NMR spectrometers, Rev. Sci. Instrum. 43 (1972) 649–653.

[19] W.-K. Rhim, D.D. Elleman, R.W. Vaughan, Analysis of multiple pulse NMR in solids, J. Chem. Phys. 59 (1973) 3740–3749.

[20] W.-K. Rhim, D.D. Elleman, L.B. Schreiber, R.W. Vaughan, Analysis of multiple pulse NMR in solids. II, J. Chem. Phys. 60 (1974) 4595–4604.

[21] A.E. Bennet, R.G. Griffin, S. Vega, Recoupling of Homo- and Heteronuclear Dipolar Interactions in Rotating Solids in: NMR Basic Principle, Springer-Verlag, Berlin, Heidelberg, 1994.

[22] D.P. Burum, M. Linder, R.R. Ernst, Low-power multipulse line narrowing in solid-state NMR, J. Magn. Reson. 44 (1981) 173–188.
[23] W.K. Rhim, D.D. Elleman, R.W. Vaughan, Enhanced resolution for solid state NMR, J. Chem. Phys. 59 (1973) 3740–3749.
[24] D.P. Burum, W.K. Rhim, Analysis of multiple pusle NMR in solids, J. Chem. Phys. 71 (1979) 944–956.
[25] M. Howhy, P.V. Bower, H.J. Jakobsen, N.C. Neilsen, A high-order and broadband CRAMPS experiment using *z*-rotational decoupling, Chem. Phys. Lett. 273 (1997) 297–303.
[26] M. Howhy, N.C. Nielsen, Elimination of high order terms in multiple pulse nuclear magnetic resonance spectrosocpy: application to homonuclear decoupling in solids, J. Chem. Phys. 106 (1997) 7571–7586.
[26] M. Veshtort, R.G. Griffin, unpublished.